Structure of an infectious mammalian prion

Allison Kraus[1,2*], Forrest Hoyt[3], Cindi L. Schwartz[3], Bryan Hansen[3], Andrew G. Hughson[2], Efrosini Artikis[2], Brent Race[2], Byron Caughey[2*]

[1]Department of Pathology, Case Western Reserve University School of Medicine, Cleveland, OH, USA

[2]Laboratory of Persistent Viral Diseases, Rocky Mountain Laboratories, National Institute of Allergy and Infectious Diseases, National Institutes of Health, Hamilton, MT 59840, USA

[3]Research Technologies Branch, Rocky Mountain Laboratories, National Institute of Allergy and Infectious Diseases, National Institutes of Health, Hamilton, MT 59840, USA

*correspondence to Allison Kraus (alk127@case.edu) or Byron Caughey (bcaughey@nih.gov)

ABSTRACT

Classical mammalian prions are assemblies of prion protein molecules that are extraordinarily transmissible, with a microgram of protein containing up to 10^8 lethal doses of infectivity[1,2]. Unlike most other pathologic and amyloidogenic proteins, prions typically contain glycolipid anchors [3] and abundant asparagine-linked glycans[4-6]. The infectious nature, complexity, and biophysical properties of prions have complicated structural analyses and stymied any prior elucidation of 3D conformation at the polypeptide backbone level[7]. Here we have determined the structure of the core of a fully infectious, brain-derived prion by cryo-electron microscopy with ~3.1 Å resolution. The purified prions are amyloid fibrils comprised of monomers assembled with parallel in-register intermolecular beta sheets and connecting chains. Residues ~95-227 of each monomer provide one rung of the ordered fibril core, with the glycans and glycolipid anchor projecting from the lateral surfaces of the fibril. The fibril ends, where prion growth occurs, are formed by single monomers in an extended serpentine combination of β-arches, a Greek key, and loops that presumably template the refolding of incoming monomers. Our results describe an atomic model to underpin detailed molecular hypotheses of how pathologic prion proteins can propagate as infectious agents, and how such propagation and associated pathogenesis might be impeded.

Main

Mammalian prion diseases include Creutzfeldt-Jakob disease, bovine spongiform encephalopathy, chronic wasting disease, and scrapie[8,9]. These and many other prion diseases are transmissible, largely untreatable, and fatal. During prion infections, prions can multiply in the host by many orders of magnitude. Although it has long been apparent that prions have high β-sheet content[1,10,11] and propagate via templated conformational conversion of the host's normal prion protein (PrP) isoform,

38 PrP^{C} [12-14], the detailed 3D structures that make this happen have been elusive. PrP-based prions are
39 comprised primarily of misfolded multimers[15,16], generically called PrP^{Sc} [8]. PrP^{C} exists primarily as a
40 heavily glycosylated, glycophosphatidylinositol (GPI)-linked and membrane-bound monomer[3-6,17] with a
41 predominantly α-helical C-terminal domain and an intrinsically disordered N-terminal domain[18]. Upon
42 conversion to PrP^{Sc}, refolding into high-β-sheet conformers[1,10,11] occurs with assembly into ordered
43 aggregates such as amyloid fibrils[19,20] and 2D crystals[21]. Although the most infectious prion particles per
44 unit protein were found to be ~600 kDa, much larger amyloid fibrils are also highly infectious[16]. PrP^{Sc}
45 multimers can induce, or seed, the conversion of PrP^{C} into PrP^{Sc} [12,22] in a manner that maintains prion
46 strain-specific PrP^{Sc} conformations[13].

47 Although the characteristics of *bona fide* PrP^{Sc} fibrils have foiled any previous determination of their
48 detailed 3D structures, low-resolution analyses have been interpreted as indicating 2 protofilaments[19,23-
49 27]. Such studies supported a plausible, but as yet unvalidated, model in which protofilaments comprised
50 of stacked 4-rung β-solenoid monomers are loosely intertwined to give a cross-section with 2-fold axial
51 symmetry[25,26]. In contrast, synthetic amyloid fibrils of full-length or N- and/or C-terminally truncated
52 bacterially-derived recombinant PrP can adopt parallel-in-register intermolecular β-sheet (PIRIBS)-based
53 architectures[28-34]. While two types of recombinant PIRIBS-based fibrils have shown detectable infectivity
54 when large amounts were injected into the brains of rodents[35,36], the observed attack rates and/or long
55 incubation periods suggest that these fibrils had extremely low titers per unit protein relative to most
56 natural prion strains. Nonetheless, these and other empirical findings have supported hypothetical
57 PIRIBS-based models for PrP^{Sc} in which a single PrP molecule spans the entire fibril axis to give an
58 asymmetric cross-section[31].

59 Importantly, following recent seminal cryo-EM-based structure determinations for various non-PrP
60 protein amyloids (e.g.[37]), high-resolution cryo-EM structures of synthetic recombinant human PrP94-178
61 (rhu94-178)[33] and PrP23-231 (rhuPrP23-231)[34] amyloid fibrils were recently solved. Each of these fibrils
62 have 2 protofilaments with PIRIBS-based proteinase K (PK)-resistant cores that are much smaller than
63 *bona fide* infectious PrP^{Sc} fibrils and, therefore, are likely to lack infectivity[38,39]. Thus, although diverse
64 types of evidence have constrained features of PrP fibril structures and their variants, no data from fully
65 infectious prions have revealed the folding of monomers within PrP^{Sc} assemblies, or allowed
66 unambiguous discrimination between widely divergent hypothetical prion models[7,9,26,31]. Here, we
67 report a high-resolution cryo-EM structure of highly infectious, brain-derived PrP^{Sc} fibrils with GPI
68 anchors and the full complement of asparagine (N)-linked glycans[3,6].

69 *PrP^{Sc} purification, infectivity, seeding activity, and negative stain EM*

70 We purified PK-resistant PrP^{Sc} fibrils from brains of clinically ill hamsters infected with the 263K scrapie
71 prion strain. Gel electrophoretic analyses of the fibril preparations indicated predominant bands at ~20-
72 32 kDa, or oligomers thereof, that comigrated with bands reacting with PrP antibodies in immunoblots
73 (Extended Data Fig. 1a). As expected, PK-treatment caused a size shift consistent with cleavages within
74 the N-terminal domain up to ~residue 90, leaving the remaining C-terminal residues intact[40,41].
75 Densitometry of protein-stained gels indicated that the preparations were ~97-98% PrP. Incubation time
76 bioassays yielded estimated titers of 5.0×10^{8} to 2.0×10^{9} 50% lethal doses per mg protein (Methods
77 and Extended Data Fig. 1d,e). Prion seeding assays[42] showed that our final manipulations immediately
78 prior to preparation of EM grids (see Methods) did not affect seeding activity (Extended Data Fig. 1b,c).
79 Negative stain transmission EM of these preparations indicated fibrillar structures (Fig. 1a). Although the

fibrils were often bundled and matted, the many isolated fibrils that we found had twists with narrow cross-over points.

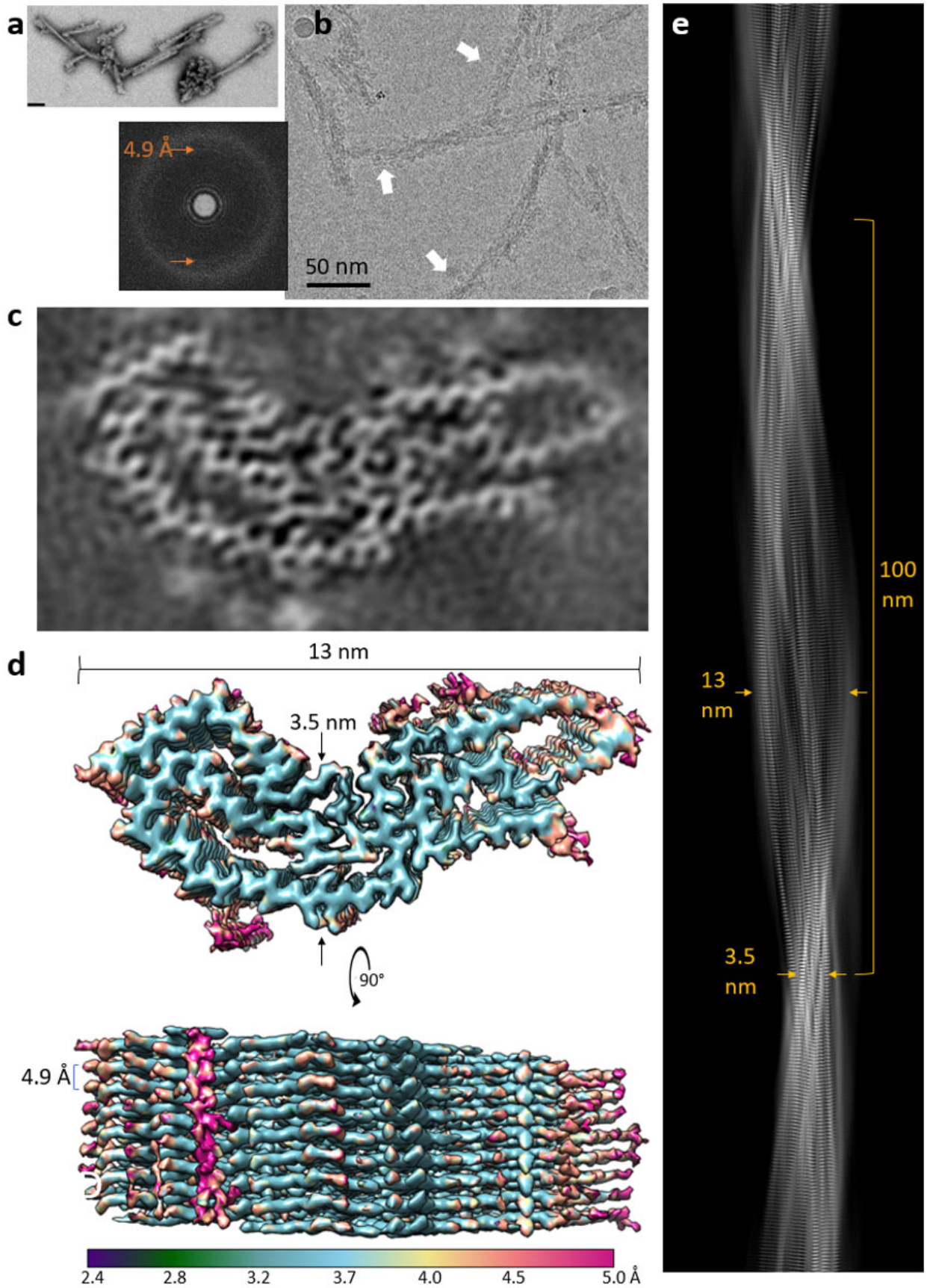
a
b
4.9 Å
50 nm
c
d
13 nm
3.5 nm
90°
4.9 Å
2.4
2.8
3.2
3.7
4.0
4.5
5.0 Å
e
100 nm
13 nm
3.5 nm

82

Fig. 1. **EM images and density maps of 263K prion fibrils**. **a**, Negatively stained transmission EM image (bar = 50 nm). **b**, Raw 2D cryo-EM image (cropped representation) with associated fast Fourier transform showing signals for regular 4.9 Å spacings (orange arrows). White arrows indicate globules. **c**, Projection of density map of fibril cross-section derived from single particle cryo-EM analysis. **d**, Surface depictions of density map with indicated dimensions and colors showing local resolutions according to bar. **e**, Projection of the fibril density map.

Tomographic analyses

Cryo-EM revealed that unstained 263K fibrils (Extended Data Fig. 2) had widths at the widest point of 13-20 nm (Extended Data Table 1). Of the isolated 263K fibrils for which twist was determinable (n=401), >99% were left-handed across 2 preparations (Extended Data Fig. 2e-h & Supplementary Information Movies 1-3). Approximately 45% of fibrils had visible ~4 nm globular features aligned along one side. The globules were spaced at 7-10 nm but could be seen along the entire length of some fibrils (Extended Data Fig. 2a-b & Supplementary Information Movies 1-3) and increased overall fibril widths by ~2-4 nm (Extended Data Table 1). Although the nature of these globules remains unclear, they might have been due in part to binding of residual detergent or other non-PrP^{Sc} molecules. Nonetheless, the single-sidedness of the globules implied an asymmetric fibril cross-section. Importantly, such asymmetry differs from the symmetrical 2-protofilament cores that have been shown for the rhuPrP23-231 fibrils[34] and rhuPrP94-178 fibrils[33], and postulated for mouse scrapie prions[25-27].

Single particle analysis and 3D image reconstruction

Additional features of PrP^{Sc} fibrils were resolved with single particle acquisition and helical reconstruction. Although this process inevitably yields a small subset of the initial particle set, several factors suggest that our results represent the preponderance of PrP^{Sc} in our fibril preparations (see Supplementary Information). Imaging and data parameters are provided in Extended Data Table 2. Fast Fourier transforms of raw 2D cryo-EM images gave weak signals indicating regular 4.9 Å spacings (Fig. 1b, offset); these signals were much stronger in transforms of particle 2D class averages (Extended Data Fig. 3d). Such spacings were also visible perpendicular to the fibril axis in images of 2D class averages. Cross-over points and multiple axial bands of density defined the twist along the fibril axis (Extended Data Fig. 3b,d). 3D classifications using the 2D particle class averages ultimately converged on a single core morphology. In contrast to previous low resolution cryo-EM-based modelling of a mouse prion strain[25,26], our 3D density map was reconstructed from the entire fibrillar cross-section (rather than halves assumed to be equivalent) without the computational imposition of symmetry about the fibril axis.

Using helical reconstruction techniques, we determined a 3.1 Å resolution map of the fibril core (Fig. 1 & 2, Extended Data Fig. 3d & Table 2). Lateral views again indicated rungs with regular 4.9 Å spacing perpendicular to the fibril axis (Fig. 1d,e). The rungs were highly uniform, which is consistent with a PIRIBS-based architecture in which each rung is the same, i.e. comprised of one PrP molecule, but inconsistent with β-solenoid models in which adjacent rungs are formed by different PrP segments. Accordingly, we built a 3D structural model by threading the PrP polypeptide backbone through densities in the fibril cross-section (Fig. 2b).

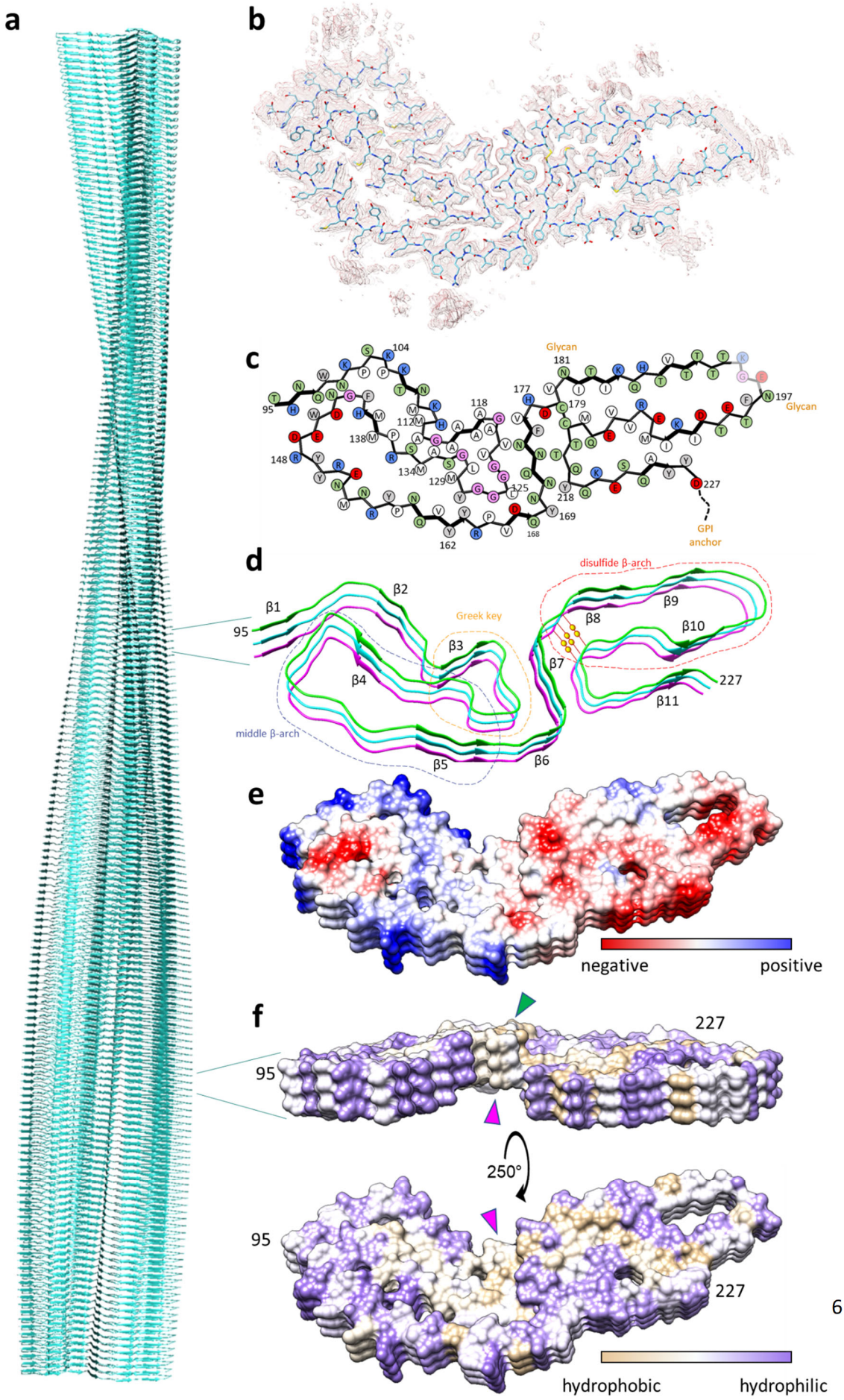
a
b
c
Glycan
Glycan
GPI anchor
d
disulfide β-arch
Greek key
middle β-arch
β1
β2
β3
β4
β5
β6
β7
β8
β9
β10
β11
95
227
e
negative
positive
f
95
227
250°
95
227
hydrophobic
hydrophilic

124 **Fig. 2. 263K prion model based on cryo-EM density map. a**, Extended fibril model as a ribbon
125 diagram. **b**, PrP residues 95-227 threaded through a cross-sectional density map (mesh). **c**,
126 Schematic depiction of fibril core showing side chain orientations relative to the polypeptide
127 backbone. Residues assigned to β-sheets in Chimera are marked by thicker backbones with
128 arrowheads. Side chains of residues 194-196 (faded) were poorly resolved. **d**, β-sheets in a
129 stacked trimeric segment of the fibril. Structural elements as labelled and disulfide bond
130 indicated by pair of yellow spheres. **e**, Coulombic charge representation. **f**, Kyte-Doolittle
131 hydrophobicity surface of fibril ends (templates) showing the protruding (green arrowhead) and
132 receding (magenta arrowheads) hydrophobic Greek key motif at opposite ends.

133 *Cross-sectional asymmetry*

134 In this structure, the cross-section is indeed asymmetric about the fibril axis (Fig. 1 & 2b-f). The well-
135 resolved fibril core, which primarily represents residues 95-227, was ~13 nm in longest dimension and
136 ~3.5 nm at its narrowest (Fig. 1e). We infer from the known attachment sites of the glycans (N181 and
137 N197) and GPI anchor (S231) that these moieties project into the solvent. However, these structures
138 were largely unresolved in the averaged image reconstruction, presumably because of their
139 heterogeneity in sequence[6] and conformation[43]. Nonetheless, the first unit of N-linked glycans, N-
140 acetylglucosamine, is consistent with the densities that are adjacent to N181 and N197 (Extended Data
141 Figs. 4 & 5). Despite published doubts that bulky glycans could fit on each rung of a PIRIBS-based core of
142 an amyloid[7], recent *in silico* studies have shown that such glycans can be accommodated[43,44]. We note
143 that the GPI anchor and N197-linked glycans are aligned asymmetrically along one edge of the fibril
144 where they might anchor and/or contribute to the globules observed in single particle imaging and
145 tomography (Fig. 1b & Extended Data Fig. 2). Another key asymmetric feature of the core is the
146 preponderance of cationic residues in the N-terminal half and anionic residues in the C-terminal half
147 (Fig. 2e). Surface hydrophobicity maps show hydrophobic zones in both halves, as well as a hydrophobic
148 bridge across the interface between the two halves (Fig. 2f). On the N terminal side, a tightly packed dry
149 zipper seals residues 96-100 to 142-145 (Fig. 3a). Other major features of the 263K structure include the
150 following:

151 *Hydrophobic "Greek key" motif*

152 A particularly hydrophobic stretch of residues ~112-134 is organized in an architecture reminiscent of
153 the "Greek key" topology in α-synuclein fibrils[45]. These residues have been shown to form species-
154 dependent PIRIBS-based β-cores in rPrP23-145 fibrils[32,46] or a much more elongated β-arch in rhuPrP94-
155 178 fibrils[33]. However, these previously observed topologies differ markedly from the 263K Greek key
156 (Figs. 2b-d & 3b and Extended Data Fig. 6a).

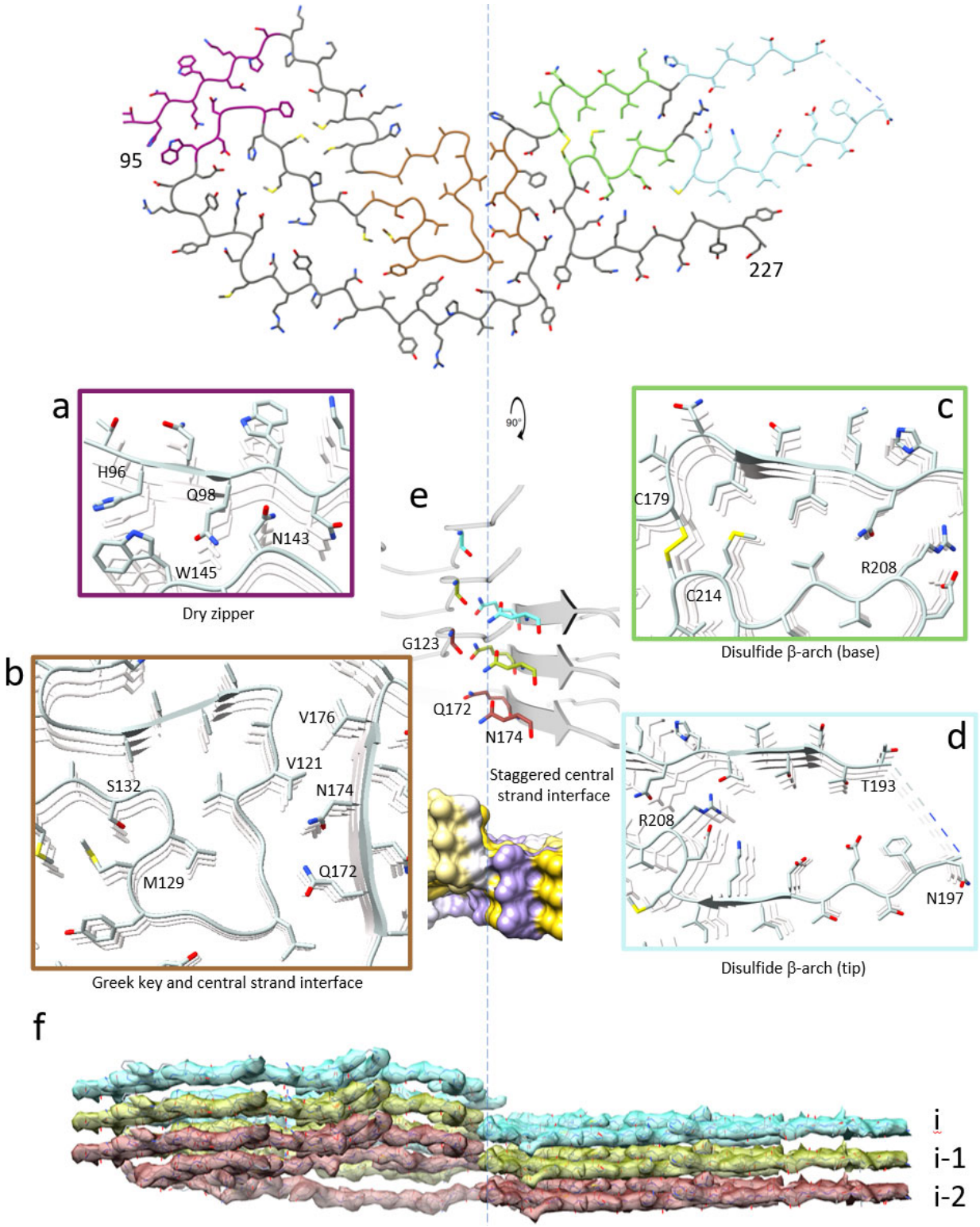

Fig. 3. Features of the 263K prion core. a, Dry zipper (purple box) formed by tight interdigitation of sidechains of residues H96, Q98 and N100 with those of W145 and N143. **b**, Tip of Greek key

motif (brown box) with hydrophobic packing of sidechains of A117, A120, V122 and L130 in the center and between V121 across a staggered interface (see below) to N174 and V176. **c**, Tight packing of hydrophobic sidechains at the base of the disulfide β-arch (green box). **d**, Wide and presumably hydrated gap between the flanks of disulfide β-arch near the tip (blue box). Dashed lines are shown in place of poorly resolved residues 194-196. **e**, Staggered interface between Greek key residues and central strand of residues 170-176 is shown with a ribbon diagram of interfacing residues and a hydrophobicity surface. **f**, Model (stick) and cryo-EM map densities (transparent surface) with monomers differentiated by color.

Middle (125-168) β-arch

Residues ~125-168 form a major hairpin or, more conventionally, β-arch[34] (Figs. 2b-d) that is related to what we had termed the "127-161 hairpin" in earlier *in silico* modelling[31]. Our initial prediction of a β-arch in this region was based on an observation that the introduction of an artificial disulfide bond into the corresponding residues of murine PrP, which covalently linked the short β1 and β2 strands of PrP^{C}, was compatible with conversion to PrP^{Sc} within scrapie-infected cells[47]. However, in the 263K structure, this middle β-arch is flipped across one or two cross-sectional axes relative to the orientations depicted in our previous hypothetical models[31].

Disulfide β-arch

263K fibrils also have a disulfide-linked β-arch between C179 and C214 (Figs. 2b-d & 3c,d). This β-arch is reminiscent of motifs that have been predicted for PIRIBS-based prions[28,29,31], or observed in rhuPrP23-231 fibrils[34]. However, in contrast to recombinant PrP fibrils, the disulfide β-arch in 263K prions contains two N-linked glycans. Also, the flanks of this arch are straighter than the β-arch in rhuPrP23-231 fibrils[34], except for a notable kink at M206-R208, and, the presumably hydrated gap between flanks near the tip of the arch is larger (Fig 3d, Extended Data Fig. 6b). The extreme C-terminal residues fold back against the flank of the disulfide loop at Y218, whereas in rhuPrP23-231 fibrils, this fold occurs at R220. Perhaps this conformational difference is influenced by sequence differences and the GPI anchor at the C-terminus of the 263K monomers, which is absent in rhuPrP23-231 fibrils.

Staggered interface between N- and C-terminal domains

Lateral views of the 263K fibril show that residues of each monomer are not entirely coplanar across the fibril cross-section and ends (Fig. 2f). At the interface between the Greek key domain and more C-terminal residues, residues ~119-135 of one monomer are most closely opposed to residues 158-177 of the i-1 and i-2 monomers (Fig. 3b,e,f). This results in uneven fibril ends with the hydrophobic Greek key motif protruding at one end and receding at the other (Fig. 2f).

Further comparisons to historical data

The 263K cryo-EM structure is consistent with a variety of other known characteristics of 263K prions or other mammalian prions that we have not already discussed above. These features include secondary structure composition, exposure (or lack thereof) of antibody epitopes, conditional exposures of minor proteolytic cleavage sites, exchange rates of PrP backbone amide protons, and the lack of clear x-ray

199 diffraction and cryo-EM signals for 10 Å inter-sheet spacings that are typical of other amyloid fibrils (see
200 Supplementary Information and Extended Data Fig. 7).

201 *Conclusions and perspectives*

202 From the cryo-EM-based density map of this highly infectious mammalian prion, the serpentine
203 threading of the polypeptide backbone of residues 95-227 and orientations of almost all of the
204 sidechains relative to the backbone were clear. Further atomistic details of sidechain conformations
205 were approximated by molecular modeling and best fit with the density map. The span of 134 residues
206 packed into the ordered 263K core is more than twice as large than in the protofilament cores of
207 previously studied recombinant PrP fibrils[32-34]. The asymmetric 263K PIRIBS-based core architecture is
208 starkly different than has been proposed for murine prion fibrils based on lower-resolution cryo-EM and
209 X-ray fiber diffraction studies[25,26], with no evidence of either β-solenoids or independent, equivalent
210 protofilaments. The middle (125-168) and disulfide β-arches were predicted in previous modelling of PrP
211 amyloids[28,29,31], but the relative orientation of these arches in the actual 263K prion structure is flipped
212 relative to our earlier speculative models. The 263K disulfide β-arch, which is heavily glycosylated, is
213 markedly different from the unglycosylated disulfide β-arch of rhuPrP23-231 fibrils[34] (Extended Data Fig.
214 6). Moreover, the attachment of glycans at N197 residues would block the head-to-head interaction
215 observed between the 2 protofilaments in the rhuPrP23-231 fibrils. The Greek key motif of hydrophobic
216 residues 113-134 is clearly distinct from those of rhuPrP23-145[32] or rhu94-178[33] (Extended Data Fig. 6).
217 Neither this Greek key motif, the middle β-arch, nor any other ordered folding in the N-terminal half of
218 the 263K prion core were resolved previously in the presumably non-infectious rhuPrP23-231 fibrils[34].
219 Thus, the additional folding in the N-terminal half of the 263K prion core may be important for
220 infectivity.

221 The C-terminal GPI anchors twist along one side of the fibril, where they would likely bind to membranes
222 *in vivo* (Fig. 4). This twisted tethering might often wrap the fibrils in membranes, impeding formation of
223 amyloid plaques, obscuring fibril visualization in tissue sections, and causing membrane distortions that
224 are pathognomonic for prion disease such as spiral membrane invaginations[17,48]. In this topology, the
225 fibril axis must run parallel to the membrane surface, with access to much of the fibril surface blocked
226 by either the N-linked glycans or the membrane. The seeding surfaces at the fibril ends would then be
227 held perpendicular to membrane surface. As postulated previously for PIRIBS-based fibril architectures
228 in general[31,49], these surfaces can be envisioned to provide a precise template for the refolding of
229 incoming monomers for the conformationally faithful propagation of PrP^{Sc} [13].

230 Comparison of the structures of PrP^{C} [50] and 263K fibrils indicates that key events in this conformational
231 conversion are the peeling of PrP^{C}'s β1-helix 1-β2 loop away from helices 2 and 3 and the unspiraling of
232 each of the helices to form the extended strands of the middle and disulfide β-arches in PrP^{Sc} (Extended
233 Data Fig. 8). This conversion also requires disruption of the β1-β2 sheet of PrP^{C}, with the associated
234 intramolecular hydrogen bonds becoming intermolecular in PrP^{Sc}. Further studies will be needed to
235 determine the order of these and other conformational changes, and the extent to which permutations
236 in PIRIBS-based architectures, and even completely different architectures such as β-solenoids, might
237 populate the range of infectious PrP-based prion strains.

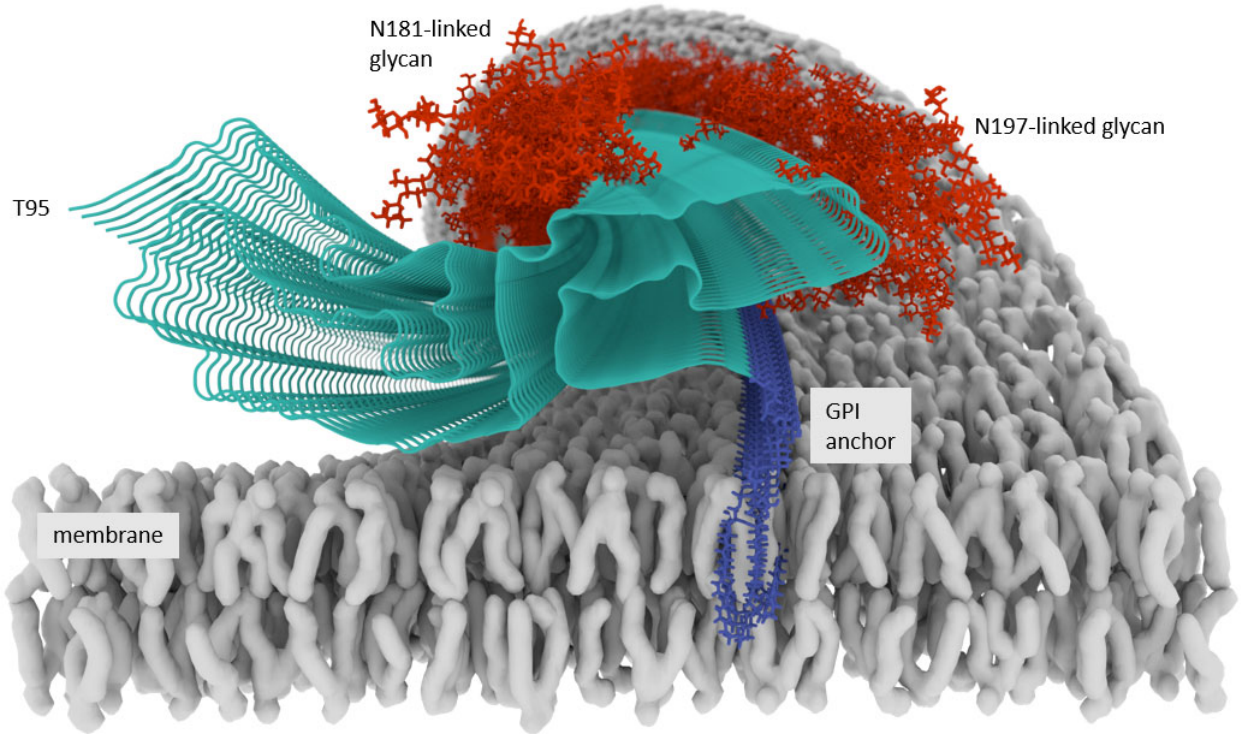

Fig. 4. Membrane-bound 263K prion model of ordered fibril core (turquoise) with hypothetical illustrations of glycans (red) and GPI anchors (blue) that were unresolved in the cryo-EM images. For simplicity, single representative structures for the N-linked glycans and GPI anchors are depicted here; however, the actual glycan and GPI anchor structures and conformations will be more varied[6]. The curl of the membrane (gray) is shown hypothetically to follow the axial twist of the GPI anchors.

Methods

Animal studies

Animals were housed at RML in an AAALAC-accredited facility. Experiments were in accordance with the NIH RML Animal Care and Use Committee approved protocols (2018-011 and 2016-039). Syrian golden hamsters were purchased from Envigo. Tg7 mice[51] for bioassays were obtained from colonies maintained at RML. To generate 263K prions for the current study, hamsters were anesthetized and intracerebrally inoculated with 30 µl of 1% 263K scrapie brain homogenate stock containing 3.8 x 10^6 50% lethal doses (LD_{50}). Animals were euthanized from 72-78 days post inoculation when consistent, advanced clinical signs of prion disease were observed. Brains were collected from these animals as described previously[52].

263K PrP^{Sc} fibril purification

PK-resistant PrP^{Sc} was purified from the hamster brain (n=20-30 per preparation) as described previously[52]. Two independent preparations (preps 1 & 2, 10 y old and fresh, respectively) were

260 analyzed with nearly indistinguishable results in all stages of this biochemical characterization and
261 imaging through tomography, single particle analysis, and 3D image reconstructions at resolutions down
262 to ~4.2 Å. However, the animal infectivity bioassay was performed only with prep 1 and, because of
263 insufficient quantity of prep 1, the final push to collect the 12,828 movies used to improve resolution
264 into the 3 Å range was performed with prep 2. SDS-PAGE and immunoblotting with a polyclonal rabbit
265 antiserum against PrP C-terminal residues (R20)[53] were performed essentially as described previously[54].
266 Immediately prior to grid preparation, fibril preparations were vortexed and allowed to sit for 10 min to
267 gravity pellet highly bundled fibrils. Aliquots were taken from the supernatant and diluted in 20 mM Tris
268 pH 7.4, 100 mM NaCl containing 0.02% amphipol 8-35 and sonicated.

269 *Bioassays of purified 263K prions*

270 To assess the infectivity of purified 263K fibrils used for cryo-EM grid preparations, fibrils from prep 1
271 were diluted in inoculation buffer (2% fetal bovine serum in phosphate buffered balanced saline). Serial
272 100-fold dilutions containing 1 µg, 10 ng, and 100 pg PK-resistant PrP^{Sc} were intracerebrally inoculated
273 as 30 µL volumes into Tg7 mice (n=7-8 per group). Infectivity titers were estimated by comparing the
274 average incubation period at each dose to a standard curve of inoculated titer vs incubation period that
275 was generated from previous end-point dilution assays of 263K hamster scrapie brain homogenate in
276 Tg7 mice. Immunohistological analyses of brain tissues were performed as described[38].

277 *Prion seeding assay (RT-QuIC) analysis*

278 Endpoint dilution analysis of the fibril preparations was conducted using RT-QuIC with recombinant
279 hamster PrP90-231 substrate as described[42].

280 *Negative stain electron microscopy*

281 Ultrathin carbon on lacey carbon support film grids (400 mesh, Ted Pella, Redding, CA) were briefly
282 glow-discharged and floated on droplets of fibril solutions. Grids were briefly washed by sequential
283 immersion in milliQ water before being negatively stained with Nano-W (2% methylamine tungstate)
284 stain (Nanoprobes, Yaphank, NY) and wicked dry. Grids were imaged at 80 kV with a Hitachi HT-7800
285 transmission electron microscope and an XR-81 camera (Advanced Microscopy Techniques, Woburn,
286 MA).

287 *Cryo-EM*

288 C-Flat 1.2/1.3 300 mesh copper grids (Protochips, Morrisville, NC) were glow-discharged with a 50:50
289 oxygen/hydrogen mixture in a Solarus 950 (Gatan, Pleasanton CA) for 10 s. Grids were mounted in the
290 tweezers for an EM GP2 plunge freezer (Leica, Buffalo Grove, IL) and a 3 µl droplet of 0.05% amphipol
291 A8-35 in phosphate buffered saline was added to the carbon surface and hand blotted, leaving behind a
292 very thin film. The tweezers were then raised into the chamber of the plunge freezer, which was set to
293 22°C and 90% humidity. 3 µl of recently sonicated sample was added to the carbon side of the grid and
294 allowed to sit for 60 s. The sample was blotted for ~4 s followed by a subsequent 3 s drain time and then
295 plunged into liquid ethane kept at -180°C. Grids were mounted in AutoGrid assemblies and then loaded
296 into a Titan Krios G3i (Thermo Fisher Scientific, Waltham, MA) with a K3 camera and BioQuantum GIF
297 (Gatan, Pleasanton, CA). Images were acquired at 0.55 Å/pixel at Super Resolution mode, 60 e-/Å2, and
298 60 total frames. A total of 12,828 movies were collected using SerialEM[55].

Cryo-electron tomography

Grids were prepared exactly as those prepared for Cryo-EM, except 1 µl of 5 nm Protein A gold (CMC, Utrecht, Netherlands) was added with 2 µl of sample on the grid before the 60 s wait time. In some cases, sample and gold fiducials were added to ultrathin carbon on lacey carbon support film (200 mesh, Ted Pella, Redding, CA) grids that were not treated with 0.05% amphipol, blotted by hand, and plunged into liquid ethane. Tilt-series were acquired bidirectional from zero every 3° between ±60° for a total dose of ~80 $e^-/Å^2$ at a pixel size of 2.87 Å using Tomography 4 software with a Falcon III camera operating in linear mode on a Krios G1 transmission electron microscope (Thermo Fisher Scientific, Waltham, MA) operating at 300 kV. Tomograms were generated with weighted back projection using IMOD [56].

Image processing

Motion correction of raw movie frames and helical reconstruction were performed with RELION 3.1[57]. CTF estimation was performed using CTFIND4.1[58]. Fibrils were picked manually (Extended Data Fig. 3a), and segments were extracted with an inter-box distance of 14.7 Å with a 370 Å box size. A second set of particles was extracted with a box size of 1280 pixels and was downscaled to a box size of 256 pixels. Reference-free 2D class averaging (Extended Data Fig. 3b) was performed on both particles sets using a regularization parameter of T = 2, in-plane angular sampling rate of 2°, a tube diameter of 200 Å, and the translational offset limited to 4.9 Å. 2D classes, from the large box size, were used to estimate the cross-over distance of the fibril. An initial 3D model was then generated, from the small box size, from multiple 2D class averages[57]. This initial model was used for 3D auto refinement with C1 symmetry, initial resolution limit of 40 Å, initial angular sampling of 3.7°, offset search range of 8 pixels, initial helical twist of -0.7°, initial helical rise of 4.8 Å, and using 20% of the segment central Z length. The output from auto refinement was used for 3D classification without allowing for image alignment to remove poorly aligned segments from auto refinement. Classes were selected for further refinement based on similarity of features in their cross-section (excluding visually low resolution and poorly aligned classes), estimated resolution, overall accuracy of rotation and translation, and Fourier completeness (Extended Data Fig. 3c). Auto-refinement was then performed while optimizing the helical twist and rise. Auto-refinement with refinement of twist and rise yielded a final map with a twist of -0.847° and rise of 4.874 Å. Iterative cycles of CTF refinement, Bayesian polishing, and auto refinement were used until resolution estimates stabilized. Post processing in RELION was performed with a soft-edged mask representing 10% of the central Z length of the fibril. Sharpening was applied with a B-factor of -31 $Å^2$. Resolution estimates were obtained between independent refined half-maps at 0.143 FSC (Extended Data Fig. 3d).

Model building

De novo building of the atomic model was carried out using Coot[59]. Assuming inclusion of residues ~90-231 into the polypeptide backbone, residue placement was initially guided by the Cys179-Cys214 disulfide bond and nearby bulky residues of 172-175 and 162-164. The remaining N and C-terminal amino acids were manually added to the model followed by targeted real-space refinement in Coot. Individual subunits were translated along the axis of the fibril to generate a stack of three consecutive subunits to maintain interactions between adjacent subunits. The translated subunits were rigid-body fit in Coot. Iterative real-space refinement and validation with Coot and Phenix[60,61] were carried out in the absence of any imposed model restraints with further local refinement in Fourier space using RefMac5[62].

341 Model validation was carried out with CaBLAM[63], MolProbity[64], and EMringer[65], and any outliers/clashes
342 identified and corrected with subsequent iterative refinements/validation as described above.
343 Additional details are as listed in Extended Data Table 2.

344

345 **Extended Data Figure Legends**

346 **Extended Data Fig. 1. 263K PrP^{Sc} preparations are protease-resistant, seed-competent, and highly**
347 **infectious. a**, Gel analysis of two independent 263K purifications. Purified 263K prions from two
348 preparations were subjected to PK digestion (PK+) and used for gel analysis and subsequent silver
349 staining or PrP immunoblotting as indicated. Untreated 263K (PK-) is shown in the first lane. **b**, Traces
350 from quadruplicate ThT readings over time for RT-QuIC reactions seeded with 2.4 fg of either the initial
351 purification of prep 1 (Total), or the same subjected to subsequent manipulations to improve fibril
352 distribution (Supernatant). Negative control reactions seeded with normal brain homogenate (NBH) at
353 10^{-4} tissue w/v dilution. **c**, Endpoint dilution RT-QuIC comparison of lag times of individual reaction wells
354 (n=4) seeded with the Total or Supernatant fractions of 263K prep 1. Data points above 30 h represent
355 reactions that failed to cross the positivity threshold within the total 30-h reaction time. Bar indicate
356 means. **d**, Kaplan-Meier survival curves after inoculation of the designated amount of 263K fibril prep 1
357 in transgenic mice (n = 7-8 per group) that overexpress hamster PrP^{C}. Survival time was determined by
358 the need to euthanize the mice according to clinical criteria for definite scrapie as referenced in
359 Methods. Dots represent individual animals euthanized at the designated time. **e**, Brain tissue from
360 animals inoculated at the highest dose was used for PrP and GFAP immunostaining, and hematoxylin
361 and eosin (H&E) staining. Consistent with the features observed with typical 263K clinical disease, PrP
362 deposition, astrogliosis (GFAP), and spongiform change were observed. Scale bar = 50 µm.

363 **Extended Data Fig. 2. Tomography of 263K prions shows left-handed fibrils and asymmetric**
364 **decoration with globules**. **a,** Tomographic slice of a fibril with globules visible on the ends, outlined with
365 white circles in **a'. b,** Another slice with globules, as marked in **b'**. **c,d,** Two slices of a 263K fibril without
366 apparent globules. **e-h,** Fibrils from 4 different tomograms showing the top, middle, and bottom slices,
367 illustrating the left-handed helix found in >99% of fibrils analyzed by tomography. Scale bars: **a-d** = 25
368 nm, **e-h** = 50 nm.

369 **Extended Data Fig. 3. Particle selection and 2D and 3D classifications in Relion**. **a**, Representative
370 micrographs are shown with examples of manually selected segments of fibrils (green) used for particle
371 extraction. **b**, Representative 2D classifications from a total of 35 used for 3D model building. **c**,
372 Representative cross-sections from 3D classes. The first and third classes (asterisks) were used for
373 subsequent model refinement, and the others of this group discarded due to visually low resolution and
374 poor alignment. **d**, Enlarged view of one of the 2D classes (highlighted in **b**) showing the 4.9Å repeated
375 spacing perpendicular to the fibril axis. Associated fast Fourier transform indicating signals at 4.9 Å
376 (inset). **e**, Fourier shell correlation plots of masked and unmasked models.

377 **Extended Data Fig. 4. Peripheral map densities** (blue) **not occupied by the polypeptide backbone of**
378 **residues 95-227**. Glycans and lipid anchor positions are labeled. Charged residues are often found next
379 to unidentified peripheral map densities that are not associated with the known (labeled) glycan or GPI
380 anchor attachment sites.
381

382 **Extended Data Fig. 5**. **Additional models with residues K194-E196 and first N-acetylglucosamine on**
383 **N181 and N197**. **a**, A polypeptide backbone inclusive of residues K194-E196 is shown within the map
384 density (mesh). **b**, The first N-acetylglucosamine (GlcNAc) units attached to the sidechains of N181 or
385 N197 are shown within map densities. **c**, Magnified cross-sectional view of N181 with the GlcNAc
386 residue. **d**, Magnified side view of the model with GlcNAc residue placement in the map densities visible
387 directly adjacent to N181. The remaining glycan extends off the fibril axis, and outside the resolved map
388 densities.

389 **Extended Data Fig. 6: Comparison of 263K Greek key and disulfide β-arches to related motifs in**
390 **previously described recombinant PrP fibrils. a**, Polypeptide backbone tracings of residues 112-141 of
391 the 263K prion Greek key compared to a Greek key-like motif modelled previously for synthetic
392 rhuPrP23-144[46] or a more extended hydrophobic core of rhuPrP94-178[33] fibrils based on solid state NMR
393 or cryo-EM data, respectively. **b**, Tracings of residues 170-227 the cryo-EM-based disulfide β-arches of
394 263K prions (current work) and synthetic rhuPrP23-231 fibrils[34]. Yellow bar indicates the disulfide bond.

395 **Extended Data Fig. 7. Antibody epitopes and proteolytic cleavage sites on 263K fibril core cross-**
396 **section. a**, Exposure of YYR and RYYR epitopes (encircled in red), one or both of which are reactive with
397 PrP^{Sc}-selective antibodies[66]. **b**, Locations of sequences that are thought to bracket elements of the PrP^{Sc}-
398 selective MAb 15B3 epitope (encircled in red). **c**, M109 and M112 (encircled in red), which are key
399 elements of the MAb 3F4 antibody epitope. **d**, Primary (large yellow arrow) and conditional minor
400 secondary (small yellow arrows) PK cleavage sites. Bottom depicts core that would remain after partial
401 unfolding and removal of residues 90-119, revealing the minor PK cleavage sites. Blue arrows mark
402 lysines in this segment.

403 **Extended Data Fig. 8**: **Domain separation and helix untwisting in conversion of PrP^{C} [67] to PrP^{Sc}.** Models
404 depicting the need for PrP^{C}'s β1-Helix 1-β2 loop (turquoise) to separate from helices 2 and 3 (purple),
405 and for each the helices to untwist into extended chains during conversion to PrP^{Sc}. This mechanism is
406 reminiscent of a previously proposed "banana peeling model"[68]. Also notable is the breakage of the
407 intramolecular backbone H-bonds of PrP^{C}'s β1-β2 sheet as they become intermolecular in PrP^{Sc} and no
408 longer in the same sheet (new positions encircled in red). Residues 23-124 of PrP^{C} are disordered in PrP^{C}
409 [67] and only residues 95-124 are depicted (orange) in the top 2 panels. Although these conformational
410 changes must occur during conversion, the order of these and other events, and whether an
411 intermediate specifically like the one depicted ever exists at any particular step, are not known. The
412 disulfide bond between C179-C214 (pair of yellow spheres) is visible only in the lower 2 panels. Note:
413 elements of these models may not be accurately matched in scale.

414 **Main References**

415 1. Caughey, B.W*., et al.* Secondary structure analysis of the scrapie-associated protein PrP 27-30 in
416 water by infrared spectroscopy. *Biochemistry* **30**, 7672-7680 (1991).
417 2. Caughey, B. & Kraus, A. Transmissibility versus Pathogenicity of Self-Propagating Protein
418 Aggregates. *Viruses* **11**(2019).
419 3. Stahl, N., Borchelt, D.R., Hsiao, K. & Prusiner, S.B. Scrapie prion protein contains a
420 phosphatidylinositol glycolipid. *Cell* **51**, 229-240 (1987).
421 4. Bolton, D.C., Meyer, R.K. & Prusiner, S.B. Scrapie PrP 27-30 is a sialoglycoprotein. *J.Virol.* **53**,
422 596-606 (1985).

423 5. Manuelidis, L., Valley, S. & Manuelidis, E.E. Specific proteins associated with Creutzfeldt-Jakob
424 disease and scrapie share antigenic and carbohydrate determinants. *Proc.Natl.Acad.Sci.USA* **82**,
425 4263-4267 (1985).
426 6. Rudd, P.M.*, et al.* Glycosylation differences between the normal and pathogenic prion protein
427 isoforms. *Proc.Natl.Acad.Sci.U.S.A.* **96**, 13044-13049 (1999).
428 7. Baskakov, I.V.*, et al.* The prion 2018 round tables (I): the structure of PrP(Sc). *Prion* **13**, 46-52
429 (2019).
430 8. Prusiner, S.B. Prions. *Proc. Natl. Acad. Sci. U.S.A.* **95**, 13363-13383 (1998).
431 9. Kraus, A., Groveman, B.R. & Caughey, B. Prions and the potential transmissibility of protein
432 misfolding diseases. *Annu. Rev. Microbiol.* **67**, 543-564 (2013).
433 10. Safar, J., Roller, P.P., Gajdusek, D.C. & Gibbs, C.J., Jr. Conformational transitions, dissociation,
434 and unfolding of scrapie amyloid (prion) protein. *J. Biol. Chem.* **268**, 20276-20284 (1993).
435 11. Pan, K.-M.*, et al.* Conversion of alpha-helices into beta-sheets features in the formation of the
436 scrapie prion protein. *Proc. Natl. Acad. Sci. USA* **90**, 10962-10966 (1993).
437 12. Kocisko, D.A.*, et al.* Cell-free formation of protease-resistant prion protein. *Nature* **370**, 471-474
438 (1994).
439 13. Bessen, R.A.*, et al.* Nongenetic propagation of strain-specific phenotypes of scrapie prion
440 protein. *Nature* **375**, 698-700 (1995).
441 14. Telling, G.C.*, et al.* Evidence for the conformation of the pathologic isoform of the prion protein
442 enciphering and propagating prion diversity. *Science* **274**, 2079-2082 (1996).
443 15. Caughey, B., Raymond, G.J., Kocisko, D.A. & Lansbury, P.T., Jr. Scrapie infectivity correlates with
444 converting activity, protease resistance, and aggregation of scrapie-associated prion protein in
445 guanidine denaturation studies. *J. Virol.* **71**, 4107-4110 (1997).
446 16. Silveira, J.R.*, et al.* The most infectious prion protein particles. *Nature* **437**, 257-261 (2005).
447 17. Caughey, B., Baron, G.S., Chesebro, B. & Jeffrey, M. Getting a grip on prions: oligomers,
448 amyloids, anchors and pathological membrane interactions. *Annu. Rev. Biochem.* **78**, 177-204
449 (2009).
450 18. Wuthrich, K. & Riek, R. Three - dimensional structures of prion proteins. *Adv.Prot.Chem.* **57**, 55-
451 82 (2001).
452 19. Merz, P.A., Somerville, R.A., Wisniewski, H.M. & Iqbal, K. Abnormal fibrils from scrapie-infected
453 brain. *Acta Neuropathol.* **54**, 63-74 (1981).
454 20. Diringer, H.*, et al.* Scrapie infectivity, fibrils and low molecular weight protein. *Nature* **306**, 476-
455 478 (1983).
456 21. Wille, H.*, et al.* Structural studies of the scrapie prion protein by electron crystallography.
457 *Proc.Natl.Acad.Sci.U.S.A* **99**, 3563-3568 (2002).
458 22. Caughey, B., Kocisko, D.A., Raymond, G.J. & Lansbury, P.T. Aggregates of scrapie associated
459 prion protein induce the cell-free conversion of protease-sensitive prion protein to the
460 protease-resistant state. *Chem.& Biol.* **2**, 807-817 (1995).
461 23. Sim, V.L. & Caughey, B. Ultrastructures and strain comparison of under-glycosylated scrapie
462 prion fibrils. *Neurobiol.Aging* **30**, 2031-2042 (2009).
463 24. Amenitsch, H., Benetti, F., Ramos, A., Legname, G. & Requena, J.R. SAXS structural study of
464 PrP(Sc) reveals ~11 nm diameter of basic double intertwined fibers. *Prion* **7**, 496-500 (2013).
465 25. Vazquez-Fernandez, E.*, et al.* The Structural Architecture of an Infectious Mammalian Prion
466 Using Electron Cryomicroscopy. *PLoS Path.* **12**, e1005835 (2016).
467 26. Spagnolli, G.*, et al.* Full atomistic model of prion structure and conversion. *PLoS Path.* **15**,
468 e1007864 (2019).
469 27. Terry, C.*, et al.* Structural features distinguishing infectious ex vivo mammalian prions from non-
470 infectious fibrillar assemblies generated in vitro. *Sci Rep* **9**, 376 (2019).

471 28. Cobb, N.J., Sonnichsen, F.D., McHaourab, H. & Surewicz, W.K. Molecular architecture of human
472 prion protein amyloid: a parallel, in-register beta-structure. *Proc Natl Acad Sci U.S.A* **104**, 18946-
473 18951 (2007).
474 29. Cobb, N.J., Apetri, A.C. & Surewicz, W.K. Prion protein amyloid formation under native-like
475 conditions involves refolding of the C-terminal alpha-helical domain. *J. Biol. Chem.* **283**, 34704-
476 34711 (2008).
477 30. Tycko, R., Savtchenko, R., Ostapchenko, V.G., Makarava, N. & Baskakov, I.V. The alpha-helical C-
478 terminal domain of full-length recombinant PrP converts to an in-register parallel beta-sheet
479 structure in PrP fibrils: evidence from solid state nuclear magnetic resonance. *Biochemistry* **49**,
480 9488-9497 (2010).
481 31. Groveman, B.R*., et al.* Parallel in-register intermolecular beta-sheet architectures for prion-
482 seeded prion protein (PrP) amyloids. *J. Biol. Chem.* **289**, 24129-24142 (2014).
483 32. Theint, T*., et al.* Species-dependent structural polymorphism of Y145Stop prion protein amyloid
484 revealed by solid-state NMR spectroscopy. *Nat Commun* **8**, 753 (2017).
485 33. Glynn, C*., et al.* Cryo-EM structure of a human prion fibril with a hydrophobic, protease-resistant
486 core. *Nat. Struct. Mol. Biol.* **27**, 417-423 (2020).
487 34. Wang, L.Q*., et al.* Cryo-EM structure of an amyloid fibril formed by full-length human prion
488 protein. *Nat. Struct. Mol. Biol.* **27**, 598-602 (2020).
489 35. Kim, J.I*., et al.* Mammalian prions generated from bacterially expressed prion protein in the
490 absence of any mammalian cofactors. *J. Biol. Chem.* **285**, 14083-14087 (2010).
491 36. Choi, J.K*., et al.* Amyloid fibrils from the N-terminal prion protein fragment are infectious. *Proc*
492 *Natl Acad Sci U S A* **113**, 13851-13856 (2016).
493 37. Goedert, M*., et al.* Tau Protein and Frontotemporal Dementias. *Adv. Exp. Med. Biol.* **1281**, 177-
494 199 (2021).
495 38. Kraus, A*., et al.* PrP P102L and nearby lysine mutations promote spontaneous in vitro formation
496 of transmissible prions. *J. Virol.* (2017).
497 39. Groveman, B.R*., et al.* Role of the central lysine cluster and scrapie templating in the
498 transmissibility of synthetic prion protein aggregates. *PLoS Path.* **13**, e1006623 (2017).
499 40. Prusiner, S.B., Groth, D.F., Bolton, D.C., Kent, S.B. & Hood, L.E. Purification and structural studies
500 of a major scrapie prion protein. *Cell* **38**, 127-134 (1984).
501 41. Hope, J*., et al.* The major polypeptide of scrapie-associated fibrils (SAF) has the same size,
502 charge distribution and N-terminal protein sequence as predicted for the normal brain protein
503 (PrP). *EMBO J.* **5**, 2591-2597 (1986).
504 42. Wilham, J.M*., et al.* Rapid End-Point Quantitation of Prion Seeding Activity with Sensitivity
505 Comparable to Bioassays. *PLoS Path.* **6**, e1001217 (2010).
506 43. Artikis, E., Roy, A., Verli, H., Cordeiro, Y. & Caughey, B. Accommodation of In-Register N-Linked
507 Glycans on Prion Protein Amyloid Cores. *ACS Chem Neurosci* **11**, 4092-4097 (2020).
508 44. Spagnolli, G*., et al.* Modeling PrP(Sc) Generation Through Deformed Templating. *Front Bioeng*
509 *Biotechnol* **8**, 590501 (2020).
510 45. Tuttle, M.D*., et al.* Solid-state NMR structure of a pathogenic fibril of full-length human alpha-
511 synuclein. *Nat. Struct. Mol. Biol.* **23**, 409-415 (2016).
512 46. Theint, T*., et al.* Structural Studies of Amyloid Fibrils by Paramagnetic Solid-State Nuclear
513 Magnetic Resonance Spectroscopy. *J. Am. Chem. Soc.* **140**, 13161-13166 (2018).
514 47. Hafner-Bratkovic, I*., et al.* Globular domain of the prion protein needs to be unlocked by domain
515 swapping to support prion protein conversion. *J.Biol.Chem.* **286**, 12149-12156 (2011).
516 48. Jeffrey, M. Review: membrane-associated misfolded protein propagation in natural
517 transmissible spongiform encephalopathies (TSEs), synthetic prion diseases and Alzheimer's
518 disease. *Neuropathol. Appl. Neurobiol.* **39**, 196-216 (2013).

519 49. Tycko, R. & Wickner, R.B. Molecular structures of amyloid and prion fibrils: consensus versus
520 controversy. *Acc Chem Res* **46**, 1487-1496 (2013).
521 50. Donne, D.G.*, et al.* Structure of the recombinant full-length hamster prion protein PrP(29- 231):
522 the N terminus is highly flexible [see comments]. *Proc.Natl.Acad.Sci.U.S.A.* **94**, 13452-13457
523 (1997).
524
525 **Additional References for Methods, Extended Data and Supplemental Information**
526
527 51. Race, R., Oldstone, M. & Chesebro, B. Entry versus blockade of brain infection following oral or
528 intraperitoneal scrapie administration: Role of prion protein expression in peripheral nerves
529 and spleen. *J. Virol.* **74**, 828-833 (2000).
530 52. Raymond, G.J. & Chabry, J. Purification of the pathological isoform of prion protein (PrPSc or
531 PrPres) from transmissible spongiform encephalopathy-affected brain tissue. in *Techniques in*
532 *Prion Research* (eds. Lehmann, S. & Grassi, J.) 16-26 (Birkhauser Verlag, Basel, 2004).
533 53. Caughey, B., Raymond, G.J., Ernst, D. & Race, R.E. N-terminal truncation of the scrapie-
534 associated form of PrP by lysosomal protease(s): implications regarding the site of conversion of
535 PrP to the protease-resistant state. *J.Virol.* **65**, 6597-6603 (1991).
536 54. Baron, G.S.*, et al.* Effect of glycans and the glycophosphatidylinositol anchor on strain
537 dependent conformations of scrapie prion protein: improved purifications and infrared spectra.
538 *Biochemistry* **50**, 4479-4490 (2011).
539 55. Mastronarde, D.N. Automated electron microscope tomography using robust prediction of
540 specimen movements. *J Struct Biol* **152**, 36-51 (2005).
541 56. Kremer, J.R., Mastronarde, D.N. & McIntosh, J.R. Computer visualization of three-dimensional
542 image data using IMOD. *J Struct Biol* **116**, 71-76 (1996).
543 57. Scheres, S.H.W. Amyloid structure determination in RELION-3.1. *Acta Crystallogr D Struct Biol*
544 **76**, 94-101 (2020).
545 58. Rohou, A. & Grigorieff, N. CTFFIND4: Fast and accurate defocus estimation from electron
546 micrographs. *J Struct Biol* **192**, 216-221 (2015).
547 59. Emsley, P., Lohkamp, B., Scott, W.G. & Cowtan, K. Features and development of Coot. *Acta*
548 *Crystallogr D Biol Crystallogr* **66**, 486-501 (2010).
549 60. Afonine, P.V.*, et al.* Towards automated crystallographic structure refinement with
550 phenix.refine. *Acta Crystallogr D Biol Crystallogr* **68**, 352-367 (2012).
551 61. Headd, J.J.*, et al.* Use of knowledge-based restraints in phenix.refine to improve macromolecular
552 refinement at low resolution. *Acta Crystallogr D Biol Crystallogr* **68**, 381-390 (2012).
553 62. Murshudov, G.N., Vagin, A.A. & Dodson, E.J. Refinement of macromolecular structures by the
554 maximum-likelihood method. *Acta Crystallogr D Biol Crystallogr* **53**, 240-255 (1997).
555 63. Williams, C.J. Duke University (2015).
556 64. Chen, V.B.*, et al.* MolProbity: all-atom structure validation for macromolecular crystallography.
557 *Acta Crystallogr D Biol Crystallogr* **66**, 12-21 (2010).
558 65. Barad, B.A.*, et al.* EMRinger: side chain-directed model and map validation for 3D cryo-electron
559 microscopy. *Nat. Methods* **12**, 943-946 (2015).
560 66. Paramithiotis, E.*, et al.* A prion protein epitope selective for the pathologically misfolded
561 conformation. *Nat.Med.* **9**, 893-899 (2003).
562 67. James, T.L.*, et al.* Solution structure of a 142-residue recombinant prion protein corresponding
563 to the infectious fragment of the scrapie isoform. *Proc.Natl.Acad.Sci.U.S.A.* **94**, 10086-10091
564 (1997).
565 68. Adrover, M.*, et al.* Prion Fibrillization Is Mediated by a Native Structural Element That Comprises
566 Helices H2 and H3. *J. Biol. Chem.* **285**, 21004-21012 (2010).

567 69. Caughey, B., Raymond, G.J. & Bessen, R.A. Strain-dependent differences in beta-sheet
568 conformations of abnormal prion protein. *J.Biol.Chem.* **273**, 32230-32235 (1998).
569 70. Smirnovas, V.*, et al.* Structural organization of brain-derived mammalian prions examined by
570 hydrogen-deuterium exchange. *Nat.Struct.Mol.Biol.* **18**, 504-506 (2011).
571 71. Speare, J.O., Rush, T.S., Bloom, M.E. & Caughey, B. The role of helix 1 aspartates and salt bridges
572 in the stability and conversion of prion protein. *J.Biol.Chem.* **278**, 12522-12529 (2003).
573 72. Korth, C.*, et al.* Prion (PrPSc)-specific epitope defined by a monoclonal antibody. *Nature* **390**, 74-
574 77 (1997).
575 73. Orru, C.D.*, et al.* Prion disease blood test using immunoprecipitation and improved quaking-
576 induced conversion. *mBio* **2**, e00078-00011 (2011).
577 74. Safar, J.*, et al.* Eight prion strains have PrP(Sc) molecules with different conformations [see
578 comments]. *Nat.Med.* **4**, 1157-1165 (1998).
579 75. Sajnani, G., Pastrana, M.A., Dynin, I., Onisko, B. & Requena, J.R. Scrapie prion protein structural
580 constraints obtained by limited proteolysis and mass spectrometry. *J.Mol.Biol.* **382**, 88-98
581 (2008).
582 76. Groveman, B.R.*, et al.* Charge neutralization of the central lysine cluster in prion protein (PrP)
583 promotes PrP(Sc)-like folding of recombinant PrP amyloids. *J. Biol. Chem.* **290**, 1119-1128
584 (2015).
585 77. Wong, C.*, et al.* Sulfated glycans and elevated temperature stimulate PrP^{Sc} dependent cell-free
586 formation of protease-resistant prion protein. *EMBO J.* **20**, 377-386 (2001).
587 78. Kocisko, D.A., Lansbury, P.T., Jr. & Caughey, B. Partial unfolding and refolding of scrapie-
588 associated prion protein: evidence for a critical 16-kDa C-terminal domain. *Biochemistry* **35**,
589 13434-13442 (1996).
590 79. McKenzie, D.*, et al.* Reversibility of scrapie inactivation is enhanced by copper. *J.Biol.Chem.* **273**,
591 25545-25547 (1998).
592 80. Eisenberg, D.S. & Sawaya, M.R. Structural Studies of Amyloid Proteins at the Molecular Level.
593 *Annu. Rev. Biochem.* **86**, 69-95 (2017).

594

595 **Acknowledgements**

596 We are very grateful to Prof. Sjors Scheres for his early advice and encouragement. We thank Dr.
597 Kunpeng Li at the CWRU cryo-EM facility for assistance in collecting cryo-EM data. We thank Ms.
598 Elizabeth Fisher for helpful suggestions and oversight of the EM facility; Dr. Dave Dorward for help with
599 preliminary negative stain TEM; Drs. Suzette Priola, Bradley Groveman, Amitava Roy and Ankit
600 Srivastava for their helpful in-house review of this manuscript; Katie Williams for help with bioassays; Dr.
601 Jacqueline Leung for assistance in analyzing related tomography data; Nancy Kurtz and Lori Lubke for
602 neuropathological slide processing; and Austin Athman and Anita Mora for graphics arts assistance. This
603 work was supported by the Intramural Research Program of the NIAID; Mary Hilderman Smith, Zoë
604 Smith Jaye, and Jenny Smith Unruh in memory of Jeffrey Smith; and the Britton Fund, Case Research
605 Institute, and CWRU School of Medicine. This work utilized the computational resources of the NIH HPC
606 Biowulf cluster (http://hpc.nih.gov).

607 **Author information**

608 *Contributions*

AK and BC supervised the project. All authors designed experiments. AH purified the PrP^{Sc}. AH and AK provided *in vitro* analyzes of PrP^{Sc} preparations. BR bioassayed PrP^{Sc} and performed neuropathological analyses. CS and AK prepared EM grids and collected EM data. CS analyzed the tomographic data. FH, CS, BH, and AK processed the cryo-EM images. FH, AK developed map parameters and FH performed class averaging and refined EM map densities in Relion. FH, BC, AK built *de novo* atomic models of PrP^{Sc}, FH and AK performed iterative refinements and map/model validation. EA performed validations for model stability and built and evaluated glycosylated and GPI-anchored models. All authors helped to prepare the manuscript.

Supplementary Information is available for this paper.

619 **EXTENDED DATA**

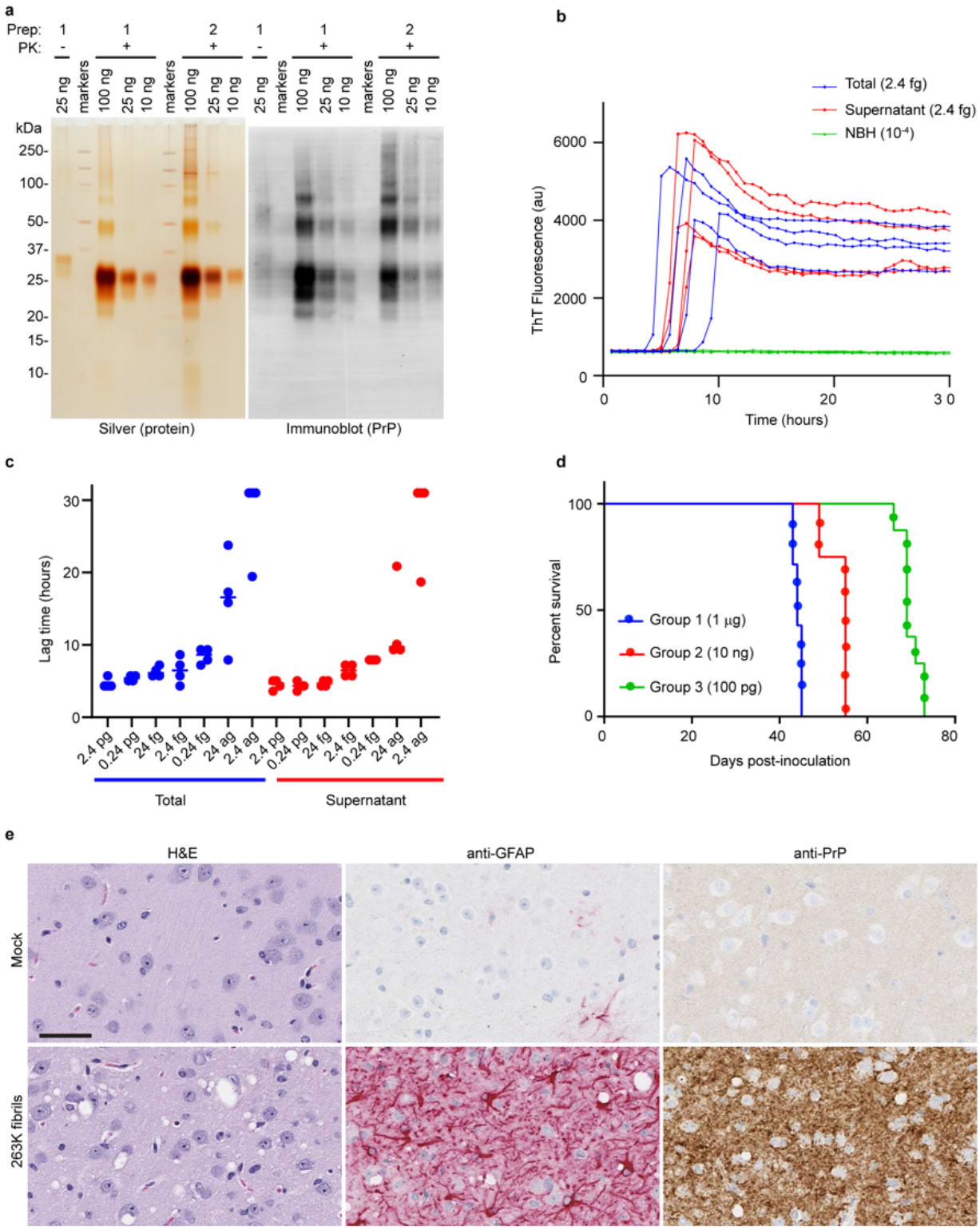

620

621

622 **Extended Data Fig. 1. 263K PrP^{Sc} preparations are protease-resistant, seed-competent, and highly**
623 **infectious. a**, Gel analysis of two independent 263K purifications. Purified 263K prions from two
624 preparations were subjected to PK digestion (PK+) and used for gel analysis and subsequent silver
625 staining or PrP immunoblotting as indicated. Untreated 263K (PK-) is shown in the first lane. **b**, Traces
626 from quadruplicate ThT readings over time for RT-QuIC reactions seeded with 2.4 fg of either the initial
627 purification of prep 1 (Total), or the same subjected to subsequent manipulations to improve fibril
628 distribution (Supernatant). Negative control reactions seeded with normal brain homogenate (NBH) at
629 10^{-4} tissue w/v dilution. **c**, Endpoint dilution RT-QuIC comparison of lag times of individual reaction wells
630 (n=4) seeded with the Total or Supernatant fractions of 263K prep 1. Data points above 30 h represent
631 reactions that failed to cross the positivity threshold within the total 30-h reaction time. Bar indicate
632 means. **d**, Kaplan-Meier survival curves after inoculation of the designated amount of 263K fibril prep 1
633 in transgenic mice (n = 7-8 per group) that overexpress hamster PrP^{C}. Survival time was determined by
634 the need to euthanize the mice according to clinical criteria for definite scrapie as referenced in
635 Methods. Dots represent individual animals euthanized at the designated time. **e**, Brain tissue from
636 animals inoculated at the highest dose was used for PrP and GFAP immunostaining, and hematoxylin
637 and eosin (H&E) staining. Consistent with the features observed with typical 263K clinical disease, PrP
638 deposition, astrogliosis (GFAP), and spongiform change were observed. Scale bar = 50 µm.

639

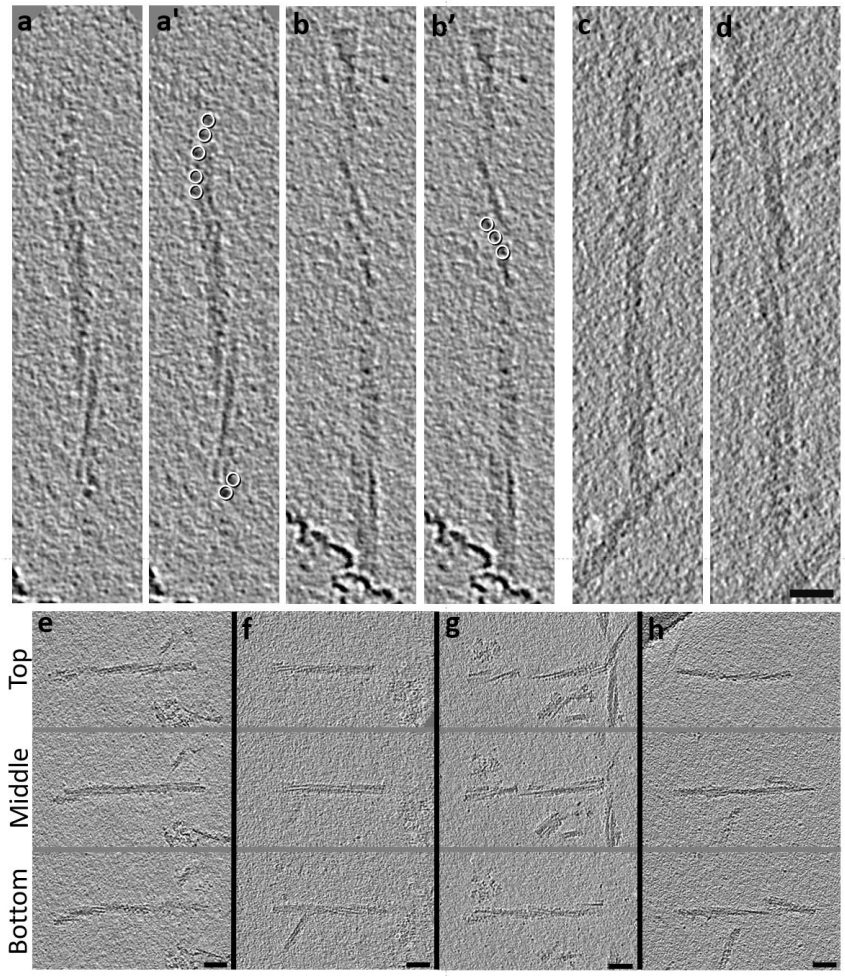

Extended Data Fig. 2. Tomography of 263K prions shows left-handed fibrils and asymmetric decoration with globules. **a,** Tomographic slice of a fibril with globules visible on the ends, outlined with white circles in **a'. b,** Another slice with globules, as marked in **b'**. **c,d,** Two slices of a 263K fibril without apparent globules. **e-h,** Fibrils from 4 different tomograms showing the top, middle, and bottom slices, illustrating the left-handed helix found in >99% of fibrils analyzed by tomography. Scale bars: **a-d** = 25 nm, **e-h** = 50 nm.

648 **Extended Data Table 1. Tomogram-based dimensions of 263K fibrils of preps 1 & 2 with and without**
649 **globules**

Fibril Prep	Globules	n	Length (nm)	Width (nm)
1	+	15	188 ±87	20 ±3
	-	64	176 ±66	16 ±3
2	+	98	137 ±54	18 ±2
	-	71	98 ±33	16 ±2

650

651 **Extended Data Table 2. Cryo-EM data, refinement, and validations**

	263K (pdb, emdb)	With 194-196
Data collection and processing		
Magnification	81,000x	
Voltage (kV)	300	
Electron dose (e-/ Å^2)	60	
Pixel size (super resolution)	0.545	
Symmetry imposed	C1	
Initial particle segments	337368	
Final particle segments	15884	
Map resolution (Å) (FSC 0.143)	3.14	
Helical rise (Å)	4.874	
Helical twist (°)	-0.847	
Map sharpening *B* factor (Å^2)	-30.98	
Model Refinement		
Initial Model	*de novo*	
R.M.S. deviations		
Bond lengths (Å)	0.011	0.011
Bond angles (°)	1.284	1.283
MolProbity score	1.26	1.35
Clash score	2.77	2.10
Rotamer outliers (%)	0	0
Ramachandran plot		
Favored (%)	96.83	94.66
Allowed (%)	3.17	5.34
Outliers (%)	0	0
EM Ringer score	5.01	4.68
Model vs. Data (CC)	0.80	0.80

652

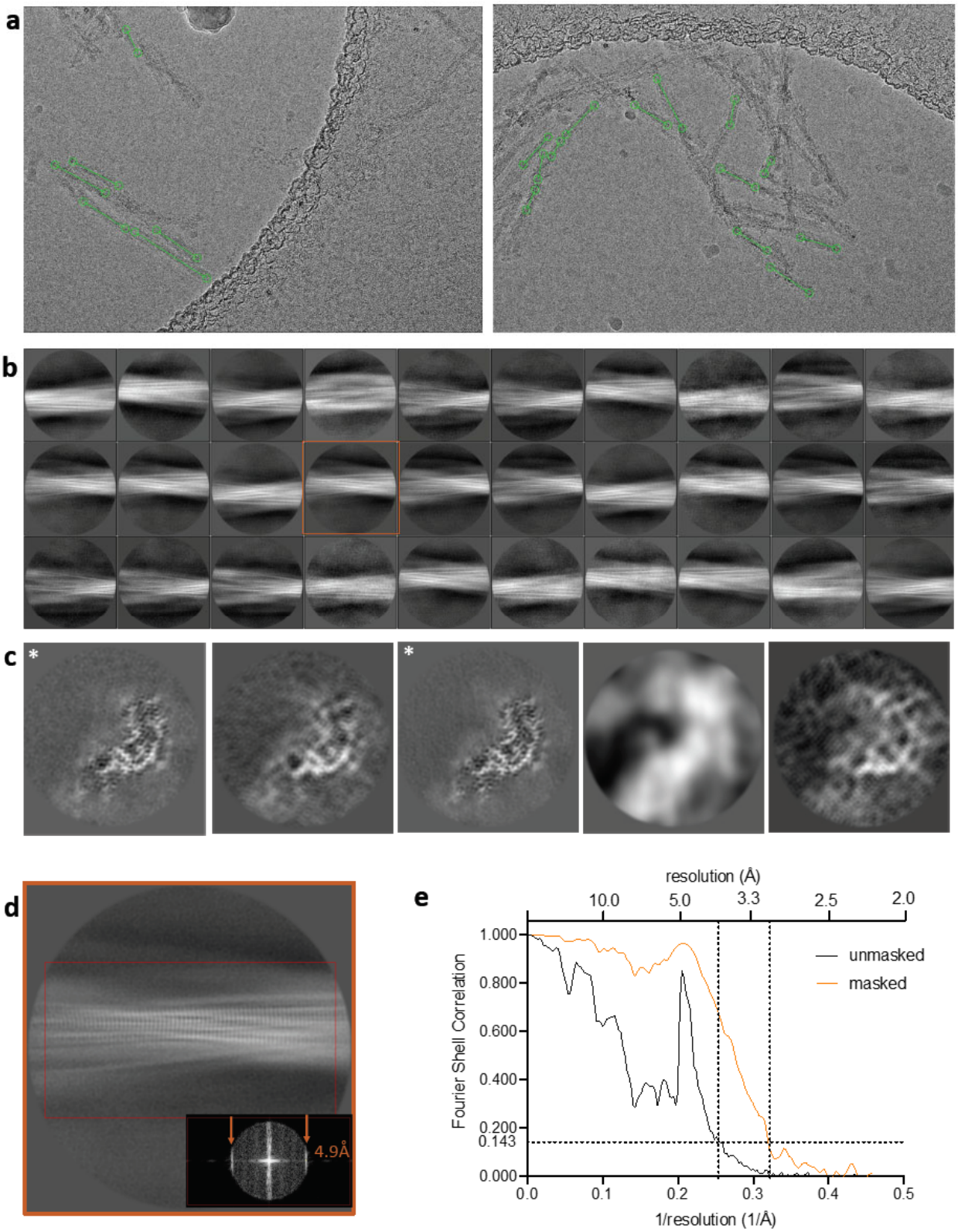
a
b
c
*
*
d
4.9Å
e
resolution (Å)
10.0
5.0
3.3
2.5
2.0
1.000
0.800
0.600
0.400
0.200
0.143
0.000
Fourier Shell Correlation
unmasked
masked
0.0
0.1
0.2
0.3
0.4
0.5
1/resolution (1/Å)

Extended Data Fig. 3. Particle selection and 2D and 3D classifications in Relion. **a**, Representative micrographs are shown with examples of manually selected segments of fibrils (green) used for particle extraction. **b**, Representative 2D classifications from a total of 35 used for 3D model building. **c**, Representative cross-sections from 3D classes. The first and third classes (asterisks) were used for subsequent model refinement, and the others of this group discarded due to visually low resolution and poor alignment. **d**, Enlarged view of one of the 2D classes (highlighted in **b**) showing the 4.9Å repeated spacing perpendicular to the fibril axis. Associated fast Fourier transform indicating signals at 4.9 Å (inset). **e**, Fourier shell correlation plots of masked and unmasked models.

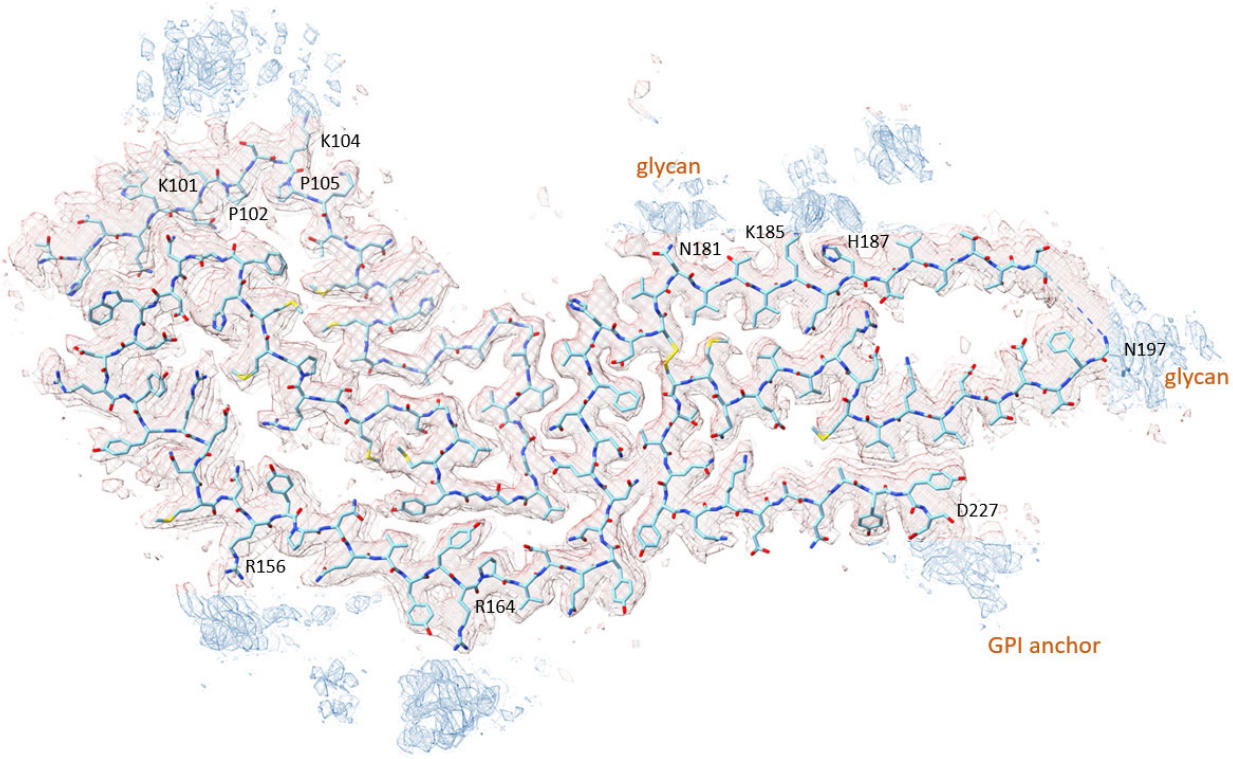

Extended Data Fig. 4. Peripheral map densities (blue) not occupied by the polypeptide backbone of residues 95-227. Glycans and lipid anchor positions are labeled. Charged residues are often found next to unidentified peripheral map densities that are not associated with the known (labeled) glycan or GPI anchor attachment sites.

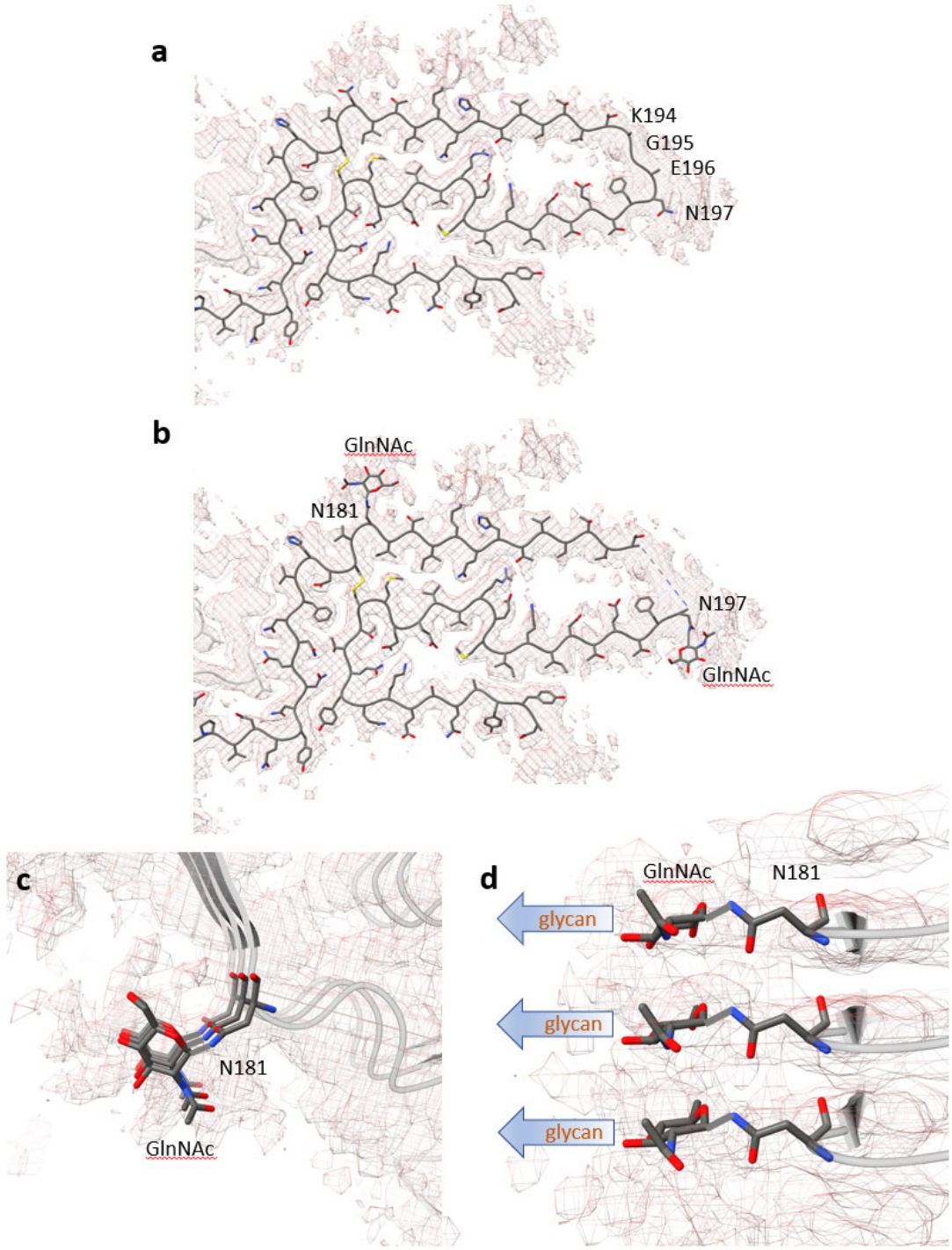

677

678 **Extended Data Fig. 5**. **Additional models with residues K194-E196 and first N-acetylglucosamine on**
679 **N181 and N197**. **a**, A polypeptide backbone inclusive of residues K194-E196 is shown within the map
680 density (mesh). **b**, The first N-acetylglucosamine (GlcNAc) units attached to the sidechains of N181 or
681 N197 are shown within map densities. **c**, Magnified cross-sectional view of N181 with the GlcNAc
682 residue. **d**, Magnified side view of the model with GlcNAc residue placement in the map densities visible
683 directly adjacent to N181. The remaining glycan extends off the fibril axis, and outside the resolved map
684 densities.

685
686

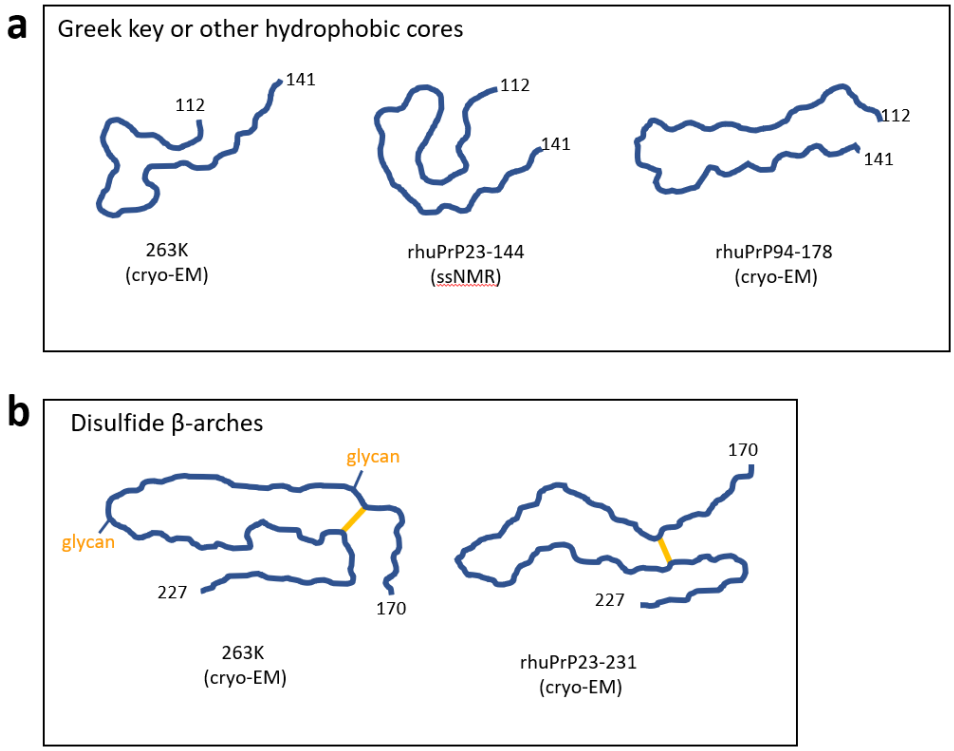

687

688 **Extended Data Fig. 6: Comparison of 263K Greek key and disulfide β-arches to related motifs in**
689 **previously described recombinant PrP fibrils. a**, Polypeptide backbone tracings of residues 112-141 of
690 the 263K prion Greek key compared to a Greek key-like motif modelled previously for synthetic
691 rhuPrP23-144[46] or a more extended hydrophobic core of rhuPrP94-178[33] fibrils based on solid state NMR
692 or cryo-EM data, respectively. **b**, Tracings of residues 170-227 the cryo-EM-based disulfide β-arches of
693 263K prions (current work) and synthetic rhuPrP23-231 fibrils[34]. Yellow bar indicates the disulfide bond.

a. YYR and RYYR epitopes

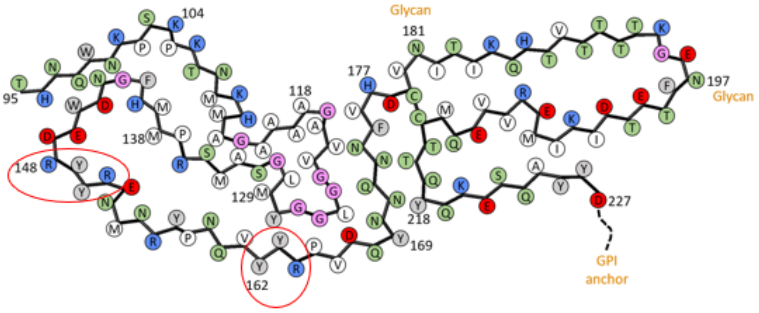

b. 15B3 epitope component

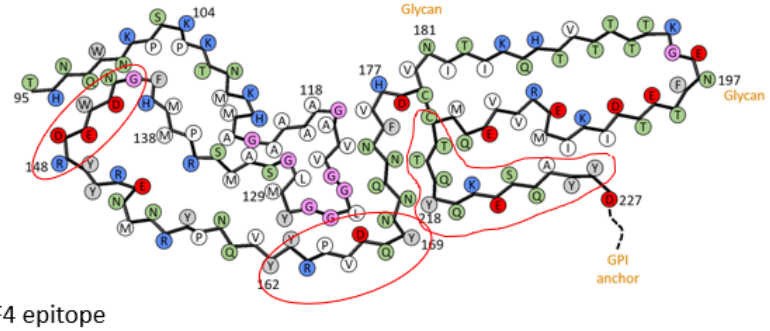

c. 3F4 epitope

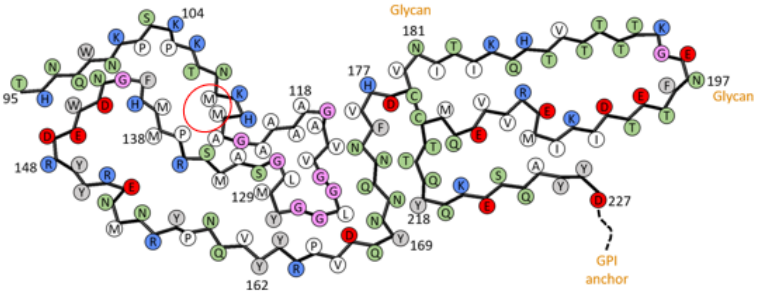

d. Proteolytic cleavage sites

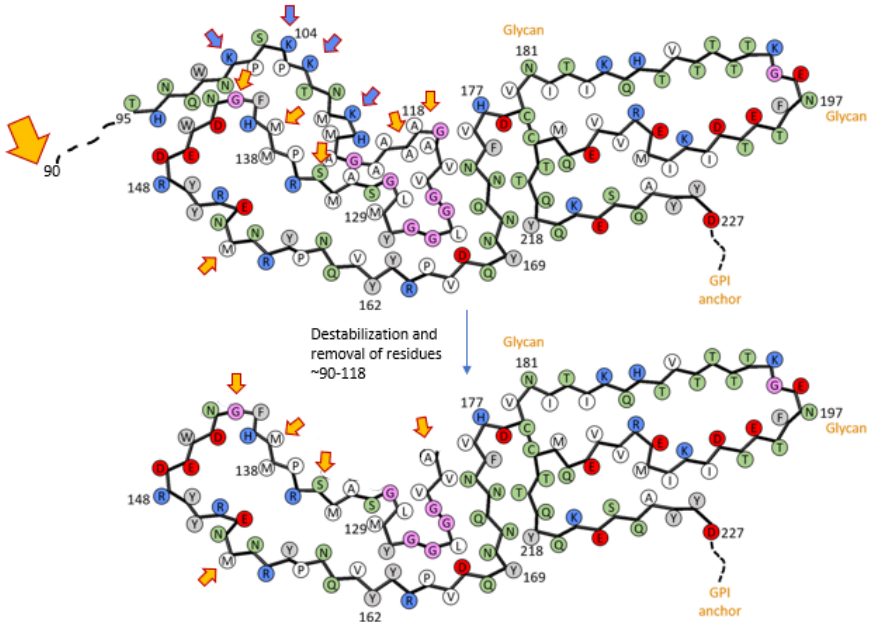

694

695 **Extended Data Fig. 7. Antibody epitopes and proteolytic cleavage sites on 263K fibril core cross-**
696 **section. a**, Exposure of YYR and RYYR epitopes (encircled in red), one or both of which are reactive with
697 PrP^{Sc}-selective antibodies[66]. **b**, Locations of sequences that are thought to bracket elements of the PrP^{Sc}-
698 selective MAb 15B3 epitope (encircled in red). **c**, M109 and M112 (encircled in red), which are key
699 elements of the MAb 3F4 antibody epitope. **d**, Primary (large yellow arrow) and conditional minor
700 secondary (small yellow arrows) PK cleavage sites. Bottom depicts core that would remain after partial
701 unfolding and removal of residues 90-119, revealing the minor PK cleavage sites. Blue arrows mark
702 lysines in this segment.

703

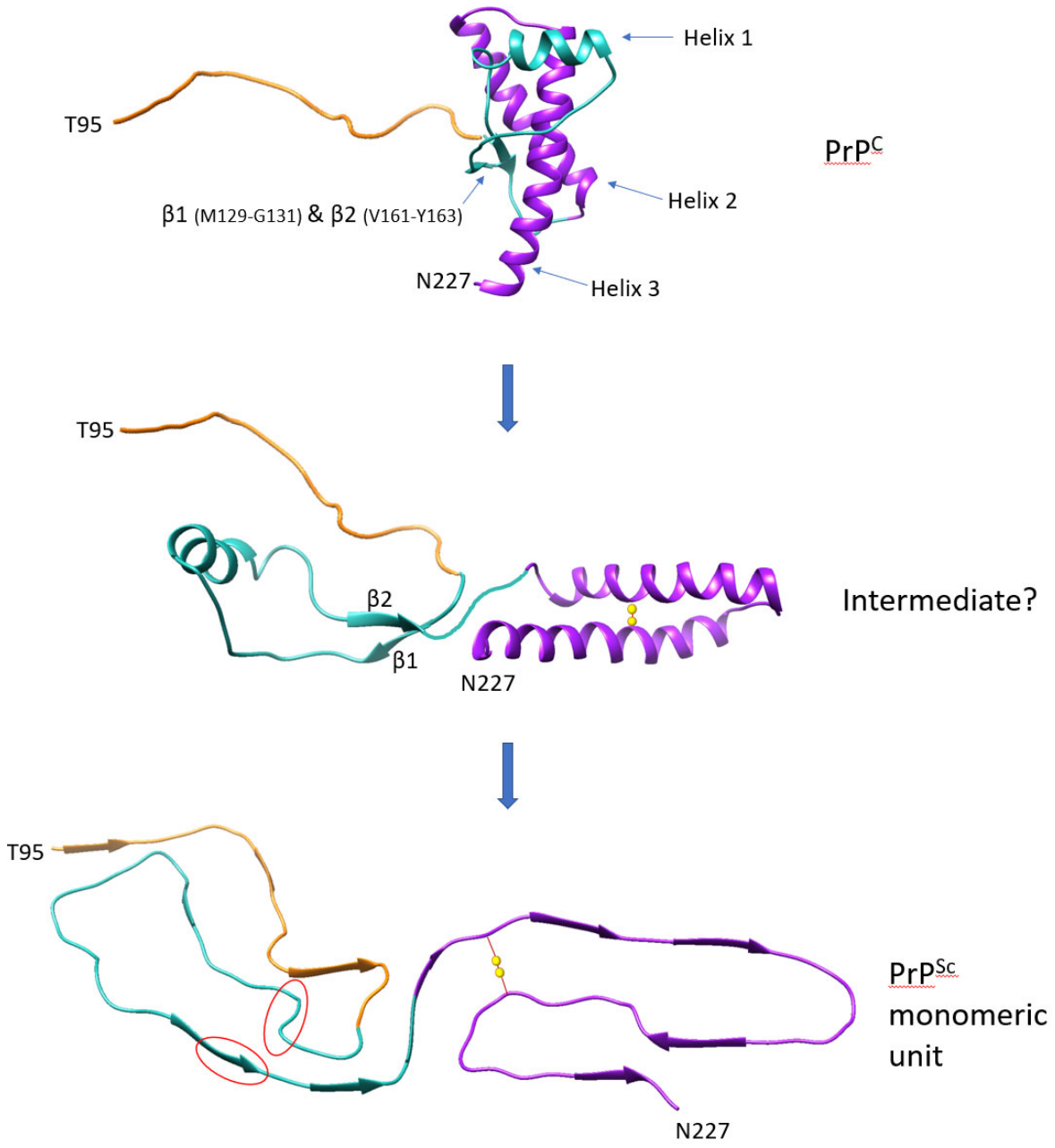

Extended Data Fig. 8: **Domain separation and helix untwisting in conversion of PrP^{C} [67] to PrP^{Sc}.** Models depicting the need for PrP^{C}'s β1-Helix 1-β2 loop (turquoise) to separate from helices 2 and 3 (purple), and for each the helices to untwist into extended chains during conversion to PrP^{Sc}. This mechanism is reminiscent of a previously proposed "banana peeling model"[68]. Also notable is the breakage of the intramolecular backbone H-bonds of PrP^{C}'s β1-β2 sheet as they become intermolecular in PrP^{Sc} and no longer in the same sheet (new positions encircled in red). Residues 23-124 of PrP^{C} are disordered in PrP^{C} [67] and only residues 95-124 are depicted (orange) in the top 2 panels. Although these conformational changes must occur during conversion, the order of these and other events, and whether an intermediate specifically like the one depicted ever exists at any individual step, are not known. The disulfide bond between C179-C214 (yellow spheres) is visible only in the lower 2 panels. Note: elements of these models may not be accurately matched in scale.